

A robust method to reach the motional quantum regime of (anti-)protons in cryogenic multi-Penning traps

Nikita Poljakov^{1*}, Jan Schaper¹, Julia-Aileen Coenders¹,
Philipp Luca Hoffmann¹, Juan Manuel Cornejo²,
Klemens Hammerer^{3,4,5}, Stefan Ulmer^{6,7}, and
Christian Ospelkaus^{1,8}

¹ Institut für Quantenoptik, Leibniz Universität Hannover, Germany

² Departamento de Física de la Materia Condensada, Universidad de Cádiz, Spain

³ Institut für Theoretische Physik, Leibniz Universität Hannover, Germany

⁴ Institut für Theoretische Physik, Universität Innsbruck, Austria

⁵ Institut für Quantenoptik und Quanteninformation, Österreichische Akademie der Wissenschaften, Austria

⁶ Ulmer Fundamental Symmetries Laboratory, RIKEN, Japan

⁷ Heinrich-Heine-Universität Düsseldorf, Germany

⁸ Physikalisch-Technische Bundesanstalt, Braunschweig, Germany

E-mail: poljakov@iqo.uni-hannover.de

February 2025

Abstract.

Sympathetic laser cooling is a key concept in precision spectroscopy and quantum state control of charged particles. Significant challenges arise in the metrologically relevant case where the effective interaction between the particles is weak and the particle to be cooled exhibits significant initial motional energy. Here we specifically address the most generally applicable case where the laser-cooled ion and the particle of interest are confined to two spatially separate potential wells with equal motional frequency for resonant enhancement of the cooling dynamics. We analyze the latter through numerical simulations and find that anharmonicities of the potential wells can prevent maintaining the resonance condition throughout the cooling process and thus inhibit a significant reduction in motional energy. We propose a cooling scheme that sweeps the trapping frequency of the potential wells. We show that this scheme enables efficient cooling from cryogenic temperatures all the way to the quantum regime of motion. As a specific application scenario, we analyze the sympathetic cooling of (anti-)protons into the quantum regime of motion for quantum-logic-spectroscopy-based tests of CPT invariance at the quantum limit in Penning traps. Nevertheless, our results and cooling strategies are generally applicable to other laser-inaccessible ion species.

Keywords: sympathetic cooling, Penning trap, simulation, antiproton, proton, CPT.

Submitted to: *Quantum Science and Technology*

1. Introduction

Full motional control of individual quantum systems, enabled through laser-cooling to the ground state of motion [1], has opened new avenues for a wide range of applications in physics, ranging from quantum information processing [2, 3] to precision metrology [4]. The ability to coherently manipulate both internal and external degrees of freedom at the single-quantum level has enabled unprecedented levels of precision in such experiments [5]. In the most general case, the particle of interest can however not be laser-cooled directly, either because of the lack of a suitable cooling transition or laser, or because direct cooling erases the internal quantum state. Sympathetic laser cooling [6] and quantum logic spectroscopy (QLS) [7, 8] address these issues by assigning coherent manipulation and spectroscopy to the ion of interest, and cooling and state detection to a “cooling” ion.

QLS, originally proposed for the (anti-)proton [7, 3], has first been demonstrated in the context of atomic clocks [8], and later successfully applied to molecular [9, 10] and highly charged ions [11], all confined in radiofrequency traps. However, not all particles can be confined as Coulomb crystals in the same potential well as is the case for the aforementioned demonstrations. In particular, the antiproton cannot be confined in a single potential well together with the readily laser-cooled atomic cations. In the most general case, sympathetic cooling would therefore be implemented with the two particles in separate potential wells, connected either directly through their Coulomb interaction [3] at close distance, or through induced image currents in a shared trap electrode [7]. Regarding the latter, the BASE collaboration [12] was able to demonstrate sympathetic laser cooling of protons by a cloud of ${}^9\text{Be}^+$ ions mediated through image currents in a shared electrode attached to a resonator [13, 14], which can provide faster cooling and lower final temperatures than current Penning-trap cooling protocols [15]. However, using that technique, it remains challenging to reach the quantum regime of motion in Penning traps. As to the former, although with both particles very close to the motional ground state, direct Coulomb coupling between separate potential wells has been demonstrated in radiofrequency traps [16, 17]. This method thus has the potential to achieve the quantum regime of motion and enable QLS in Penning traps [18, 19].

These advancements are particularly relevant for high-precision experiments, such as those conducted by the BASE collaboration in their search for discrepancies between protons and antiprotons to test the CPT (Charge-Parity-Time reversal) theorem [20]. BASE is performing high-precision measurements of the charge-to-mass ratio [21] and g -factors of the (anti-)proton [22, 23] in advanced cryogenic multi-Penning traps, and recently demonstrated coherent spin spectroscopy of an antiproton [15], enabling further improvements in the g -factor precision. A possible route for improving both precision and sampling rates in such experiments could be achieved by applying QLS techniques to Penning traps, where the preparation of the (anti-)proton in the motional ground state

via sympathetic cooling is a key requisite. Ultimately, extending these techniques to a wider range of ion species could have a significant impact on high-precision experiments in Penning traps.

In this paper, we analyze the dynamics of sympathetic laser cooling in a realistic double-well potential, focusing on the scenario of cooling of an (anti-)proton through coupling to a laser-cooled ${}^9\text{Be}^+$ ion. An implementation in any metrologically relevant scenario will, however, have to take into account that the particle of interest that cannot be directly laser-cooled may have a comparatively large initial axial motional energy after thermalizing with the cryogenic environment at 4 K. To address that, we analyze the energy range of the harmonic region of the trapping potential and quantify the stability of energy transfer against voltage fluctuations. We show that, due to trap anharmonicities and limited voltage stability, sympathetic cooling is inefficient for higher-energy particles in the static double-well potential. We therefore propose a frequency-sweeping scheme that exploits these anharmonicities to enhance cooling.

The manuscript is organized as follows. The ‘‘Experimental setup’’ section describes a multi-Penning trap stack and measurement techniques that can be implemented for the (anti-)proton- ${}^9\text{Be}^+$ coupling. The ‘‘Method’’ section introduces the mathematical and numerical framework for simulating the trapping potentials and coupling dynamics. The ‘‘Results and Discussion’’ section presents the simulation results, including the ground-state cooling protocol. Finally, the ‘‘Conclusion’’ section provides a summary and an outlook.

2. Experimental setup

A Penning trap confines charged particles using a combination of a strong, homogeneous magnetic field \vec{B} in the axial direction and a static electric quadrupole potential. The trapped particle exhibits three independent harmonic modes of motion: two radial modes — the modified cyclotron and magnetron motions with frequencies ω_+ and ω_- , respectively — perpendicular to the magnetic field, and an axial motion parallel to it with a frequency ω_z . These eigenmotions can be related to the free cyclotron frequency ω_c by the invariance theorem, $\omega_c = \sqrt{\omega_+^2 + \omega_-^2 + \omega_z^2} = q|\vec{B}|/m$ [24], where q is the charge, B the magnetic field strength, and m the particle mass.

Fig. 1a shows a schematic of a multi-Penning trap in which the sympathetic cooling scheme of the (anti-)proton via direct Coulomb interaction could be implemented. The trap stack consists of different trapping regions denoted with different colors. In our setup [25, 26, 27], we employ ${}^9\text{Be}^+$ as the cooling ion, as it is the laser-accessible species with the closest mass to the (anti-)proton. In the ‘‘Beryllium trap’’ (shown in red), a single ${}^9\text{Be}^+$ ion is loaded using a pulsed 532 nm ablation laser and a 235 nm photoionization laser, and is cooled to the motional ground state using a resolved Raman sideband cooling scheme [28]. It has been shown that a proton can be reliably loaded using the same ablation laser on a tantalum target [29, 30], which is placed in the ‘‘Proton trap’’ (green). The proton will be detected and cooled to 4 K using an axial

resonator in the “Precision trap” (white) [31]. An antiproton could be injected from a transportable Penning trap system of the BASE-STEP experiment at CERN [32]. Using fast adiabatic transport [33, 34], both ${}^9\text{Be}^+$ and an (anti-)proton could be transported into the desired double-well potential of a microfabricated trap section, called the “Coupling trap” [25] (yellow) (see Fig. 1b), where our ground-state cooling method of the (anti-)proton will be employed. After the coupling, the ${}^9\text{Be}^+$ ion can be transported into the Beryllium trap to measure its temperature and to re-initialize it in the ground state, while the (anti-)proton can be stored on the other side of the Coupling trap.

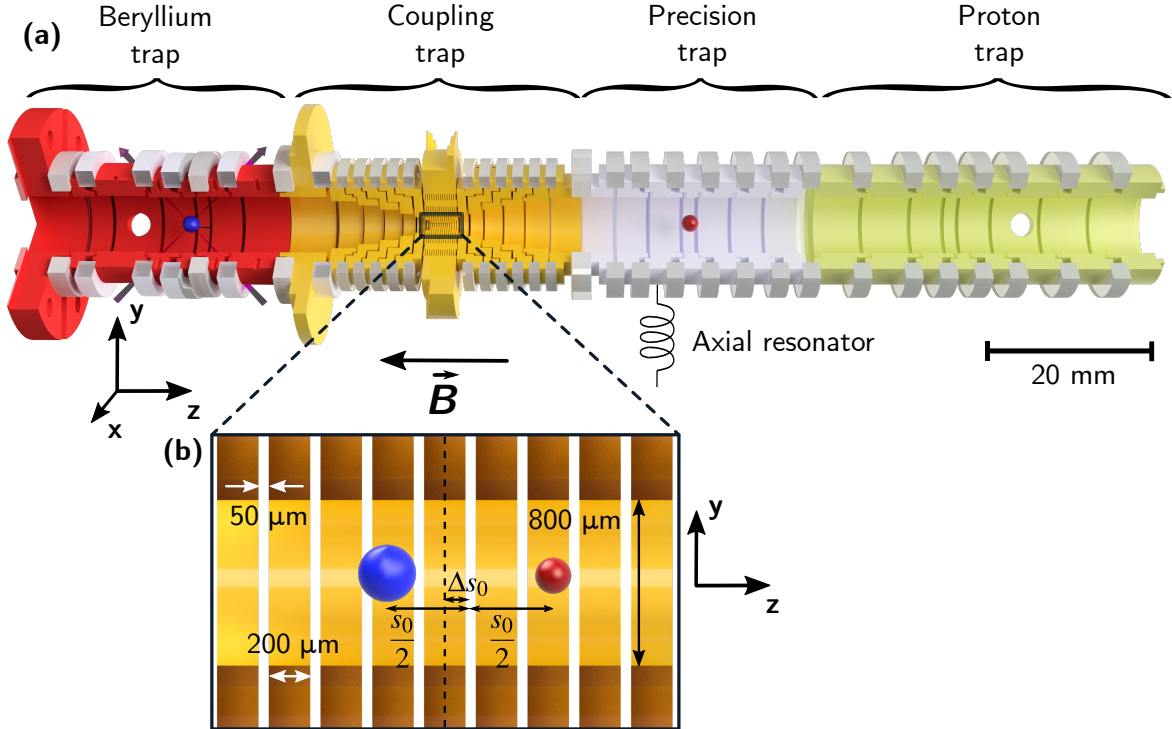


Figure 1: **Multi-Penning trap.** **a)** Cross-sectional view of an exemplary multi-Penning trap design for the coupling experiments, with trap sections shown in different colors. A ${}^9\text{Be}^+$ ion is depicted in blue and an (anti-)proton in red. The inner trap surface is circularly symmetric around the trap axis. The macroscopic trap electrodes have inner diameters of 9 mm and are made of gold-plated, oxygen-free high thermal conductivity copper. An axial resonator, consisting of a superconducting coil and a cryogenic amplifier, is connected to a precision trap electrode for (anti-)proton detection and 4 K cooling. Purple arrows illustrate the Raman beams used for cooling and temperature measurement of the ${}^9\text{Be}^+$ ion. **b)** Detailed cross-sectional view of the Coupling trap, consisting of nine microfabricated electrodes. The positions of the (anti-)proton and ${}^9\text{Be}^+$ ion are shown, along with the particle separation s_0 and offset Δs_0 relative to the central electrode. Further details are provided in the text.

The Coupling trap has an inner diameter of 800 μm and is composed of 200 μm -thick electrodes separated by 50 μm . The electrodes are structured through selective laser-induced etching of a fused-silica substrate, followed by lithographic processing, and completed by electroplating to deposit the gold layer. The remaining unplated fused silica forms a C-shaped support structure that enables self-aligning stacking of the electrodes. The fabrication of the coupling trap is discussed in detail in [35]. The trap comprises nine electrodes, providing nine independent degrees of freedom. Its compact geometry reduces the constraints associated with shaping the double-well potential, as discussed in the following section.

3. Method

To simulate double-well potentials for the sympathetic cooling of the (anti-)proton, we first model the Coupling trap electrodes described above in COMSOL [36]. Using the finite element method, we obtain electrostatic potentials $\phi_i(z)$ and electric fields $\frac{\partial\phi_i}{\partial z}(z)$ along the trap axis z for each electrode i individually set to 1 V, and other electrodes $\neq i$ set to 0 V. These values are then used to solve the following matrix equation [37, 33] for the voltages V_1, V_2, \dots, V_n applied to $n = 9$ electrodes,

$$\begin{pmatrix} \frac{\partial\phi_1}{\partial z}|_{z=z_{a,0}} & \frac{\partial\phi_2}{\partial z}|_{z=z_{a,0}} & \cdots & \frac{\partial\phi_n}{\partial z}|_{z=z_{a,0}} \\ \frac{\partial\phi_1}{\partial z}|_{z=z_{b,0}} & \frac{\partial\phi_2}{\partial z}|_{z=z_{b,0}} & \cdots & \frac{\partial\phi_n}{\partial z}|_{z=z_{b,0}} \\ \frac{\partial^2\phi_1}{\partial z^2}|_{z=z_{a,0}} & \frac{\partial^2\phi_2}{\partial z^2}|_{z=z_{a,0}} & \cdots & \frac{\partial^2\phi_n}{\partial z^2}|_{z=z_{a,0}} \\ \frac{\partial^2\phi_1}{\partial z^2}|_{z=z_{b,0}} & \frac{\partial^2\phi_2}{\partial z^2}|_{z=z_{b,0}} & \cdots & \frac{\partial^2\phi_n}{\partial z^2}|_{z=z_{b,0}} \end{pmatrix} \begin{pmatrix} V_1 \\ V_2 \\ \vdots \\ V_n \end{pmatrix} = \begin{pmatrix} 0 \\ 0 \\ \frac{m_a\omega_a^2}{q_a} \\ \frac{m_b\omega_b^2}{q_b} \end{pmatrix}, \quad (1)$$

where $z_{a,0}$ and $z_{b,0}$ denote the positions of the double-well potential minima for charged particles a and b , m_a and m_b are their masses, q_a and q_b are their charges, ω_a and ω_b are their angular oscillation frequencies. To minimize anharmonicities, we set the third- and fourth-order derivatives of the potential at its minima to zero; these terms are omitted in Eq. 1 for brevity. The solution with the smallest voltages is obtained using the Moore-Penrose inverse [38]. Using the superposition principle, the resulting voltages are combined to construct the double-well potential,

$$\Phi(z) = \sum_{i=1}^n V_i \phi_i(z). \quad (2)$$

Examples of the resulting double-well potentials are shown in Fig. 2a for the proton and in Fig. 2b for the antiproton. The potentials are asymmetric due to the 9:1 mass ratio of the ${}^9\text{Be}^+$ ion and the (anti-)proton. For the proton, the well depth is determined by the barrier height between the proton and the ${}^9\text{Be}^+$ ion. For the antiproton, which carries a negative charge, there is no barrier between it and the ${}^9\text{Be}^+$ ion; however, a finite barrier exists on the opposite side of the well.

We simulate sympathetic cooling of the (anti-)proton in the double-well potential using the Verlet method [39], which is symplectic and thus provides good energy

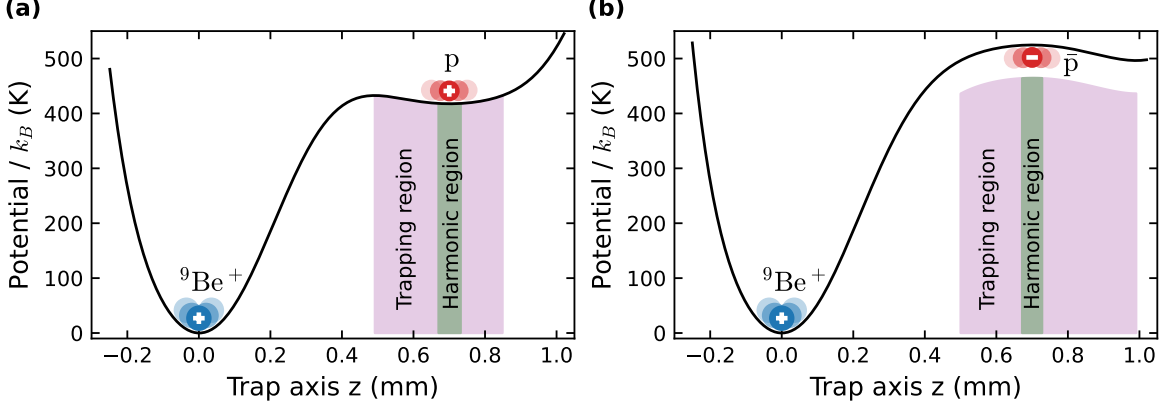


Figure 2: **Double-well potential.** **a)** Proton coupled with a ${}^9\text{Be}^+$ ion. **b)** Antiproton coupled with a ${}^9\text{Be}^+$ ion. The double-well potentials were generated using potential minima separation $s_0 = 0.7\text{ mm}$ and axial trap frequency $f = \omega/2\pi = 500\text{ kHz}$ for both potential minima. The antiproton potential well is inverted due to its negative charge. The purple shaded region indicates the positions where the (anti-)proton can be trapped, while the green shaded region represents positions where it experiences a harmonic potential. The energy ranges of the trapping and harmonic regions are described in more detail in Fig. 4.

conservation. The simulation timestep is chosen in the range of 10 ns to 50 ns, which oversamples the axial oscillation period by at least a factor of 100 to ensure accurate energy conservation. At every timestep, we evaluate the force that particle a experiences due to the Coulomb force from particle b and electrostatic force of the trap,

$$F_a(z_a, z_b) = \frac{1}{4\pi\epsilon_0} \frac{q_a q_b}{(z_a - z_b)^2} + q_a \left. \frac{\partial\Phi}{\partial z} \right|_{z=z_a}, \quad (3)$$

where z_a and z_b are particle positions, ϵ_0 is the vacuum permittivity, and $\left. \frac{\partial\Phi}{\partial z} \right|_{z=z_a}$ is the electric field of the double-well potential experienced by the particle a . An analogous calculation is performed for particle b . Due to the second-order term of the Taylor expansion of the Coulomb potential [16], the charged particles can be described as coupled harmonic oscillators behaving like oscillating masses connected by a spring if the resonance condition $\omega_a \approx \omega_b$ is satisfied. Therefore, as the particles oscillate in their respective potential wells, their energies are exchanged after the exchange time [16],

$$\tau_{ex} = \frac{2\pi^2\epsilon_0 s_0^3 \sqrt{m_a m_b} \sqrt{\omega_a \omega_b}}{q_a q_b}. \quad (4)$$

In our simulations, the total energy of the particles during the exchange process is evaluated as the sum of their kinetic and electrostatic potential energies along the trap axis z . We consider only the axial motion, because the radial amplitude of the (anti-)proton can be reduced to $\sim 1\ \mu\text{m}$ by coupling the radial and axial motions using radiofrequency pulses applied to the trap electrodes [40, 41]. For the ${}^9\text{Be}^+$ ion, the radial

amplitude can be reduced to $\lesssim 1 \mu\text{m}$ using laser cooling and axialization techniques [42]. Consequently, for both particles, the radial amplitude is negligible compared to s_0 .

In this work, we present two numerical studies: 1) harmonic coupling (see subsection 4.1) and 2) frequency sweep (see subsection 4.2). The numerical sequences of both studies are illustrated in Fig. 3. For the harmonic coupling study, we consider a time-independent double-well potential in which both particles are confined to harmonic regions around their respective potential minima. The ${}^9\text{Be}^+$ ion is initialized in its motional ground state, while the (anti-)proton is prepared with an initial energy $E_{p/\bar{p},\text{init}}$. During the coupling process, the ${}^9\text{Be}^+$ ion is not subjected to laser cooling. From the second-order term of the Taylor expansion of the Coulomb potential, it follows that if $m_a \neq m_b$, the interaction induces an angular frequency shift $\Delta\omega$ between the two oscillating particles,

$$\Delta\omega = \left(\frac{1}{m_a} - \frac{1}{m_b} \right) \frac{q_a q_b}{4\pi\epsilon_0\omega s_0^3}. \quad (5)$$

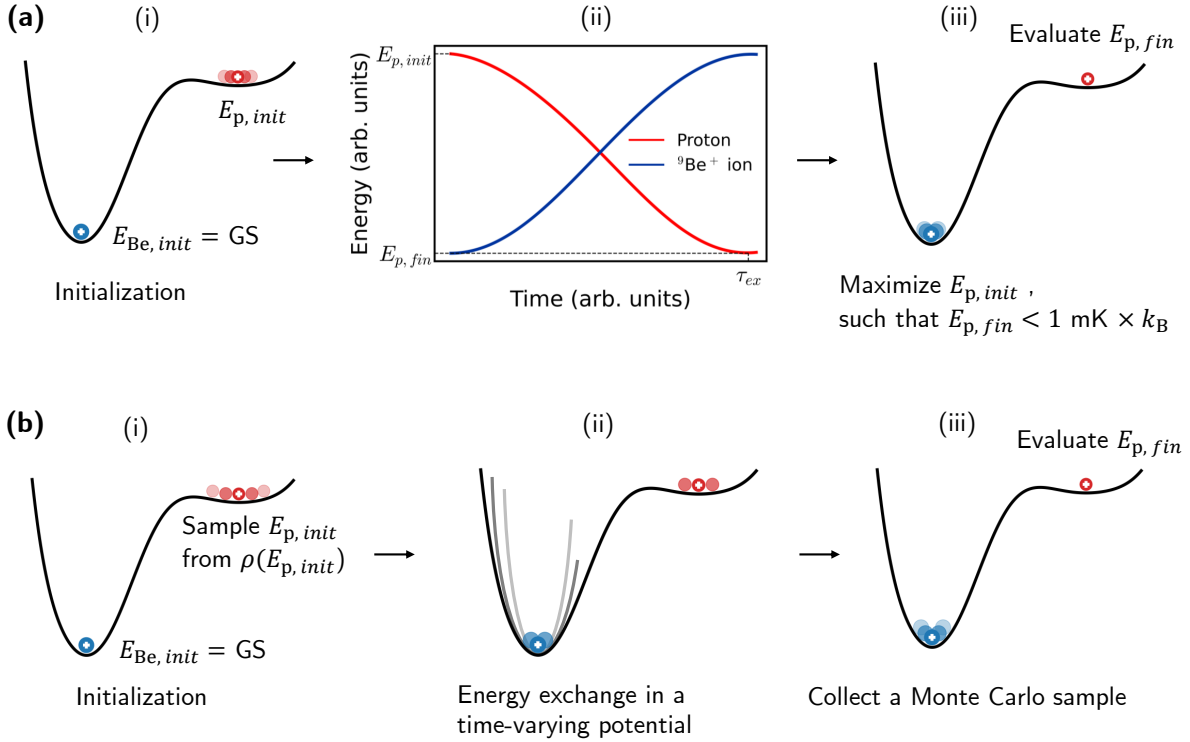


Figure 3: **Simulation sequence.** (a) Harmonic coupling. (b) Frequency sweep. The simulation sequences are shown using a proton as an example; the same studies are performed for the antiproton. Both subfigures are divided into three steps: i) initialization of the (anti-)proton with energy $E_{p/\bar{p},\text{init}}$ and preparation of the ${}^9\text{Be}^+$ ion in its motional ground state (GS); ii) energy exchange between the particles; iii) analysis of the final (anti-)proton energy $E_{p/\bar{p},\text{fin}}$. The plot in subfigure (a.ii) shows an example of the energy evolution of the (anti-)proton and ${}^9\text{Be}^+$ ion during the coupling process in the time-independent double-well potential.

The derivation of this formula is presented in Appendix A. To maintain the resonance condition, the curvatures of the potential wells near their respective minima are chosen such that the oscillation frequencies of the two trapped particles are detuned by $\Delta\omega$. The simulation is run for at least the exchange time τ_{ex} , during which the particle energy evolution is calculated. An example of this evolution is shown in Fig. 3a and exhibits the sinusoidal behavior expected for coupled harmonic oscillators. Finally, the minimum (anti-)proton energy $E_{p/\bar{p},fin}$ is analyzed. The procedure is repeated while increasing $E_{p/\bar{p},init}$ until the condition $E_{p/\bar{p},fin} < 1 \text{ mK} \times k_B$ is no longer satisfied. In this way, the boundary of the harmonic region accessible to the (anti-)proton is estimated.

For the frequency sweep study, we consider a time-dependent potential, where the (anti-)proton is not necessarily confined to the harmonic region near its potential minimum, as it may possess a larger initial energy $E_{p/\bar{p},init}$ than in the harmonic coupling study. To calculate the (anti-)proton's initial axial energy, $E_{p/\bar{p},init}$, we model it as a canonical ensemble in thermal contact with the axial resonator coil, which acts as a thermal reservoir at $T_z = 4 \text{ K}$. Accordingly, the (anti-)proton is initialized by taking random samples from the Boltzmann distribution, given by

$$\rho(E_{p/\bar{p},init}) = \frac{1}{k_B T_z} \exp[-E_{p/\bar{p},init}/(k_B T_z)], \quad (6)$$

where k_B is the Boltzmann constant. The ${}^9\text{Be}^+$ ion is again initialized in its motional ground state. We select a set of ${}^9\text{Be}^+$ ion trapping frequencies for the sweep, and find the corresponding voltages by solving Eq. 1. To obtain the intermediate frequency values, we perform linear interpolation of the voltages. During the frequency sweep, the energy is exchanged between the particles, and the final (anti-)proton energy $E_{p/\bar{p},fin}$ is evaluated at the last timestep of the sweep and recorded as a Monte Carlo sample. Further details about the numerical studies are discussed in the following section.

4. Results and Discussion

Here, we present the results of harmonic coupling and frequency sweep simulations which are subsequently combined to form a sympathetic cooling scheme.

4.1. Harmonic coupling

We study the cooling dynamics of the ${}^9\text{Be}^+$ -(anti-)proton coupling in time-independent double-well trapping potentials that can be produced in the Coupling trap using different trapping parameters. As shown in Tab. 1, we optimize the positions of particles with respect to the electrodes by introducing an axial offset Δs_0 , such that it maximizes the energy that can be cooled using the harmonic region of the (anti-)proton potential.

We estimate the maximum energy from which an (anti-)proton can be cooled to below 1 mK, as shown in Figs. 4a and 4b. In our analysis, we restrict the parameters to those achievable with electrode voltages below 10 V, which sets an upper limit on the axial trap frequency $f = \omega/2\pi$ for each value of s_0 in the plots. Increasing both f and

Table 1: Optimized offsets, $\Delta s_{0,p}$ and $\Delta s_{0,\bar{p}}$, corresponding to the maximum harmonicity of the potential for the proton and antiproton, respectively. The offset is defined as the distance between the central electrode and the midpoint between the particles, as illustrated in Fig. 1b.

s_0 (mm)	$\Delta s_{0,p}$ (μm)	$\Delta s_{0,\bar{p}}$ (μm)
0.6	50	50
0.7	32	53
0.8	95	88

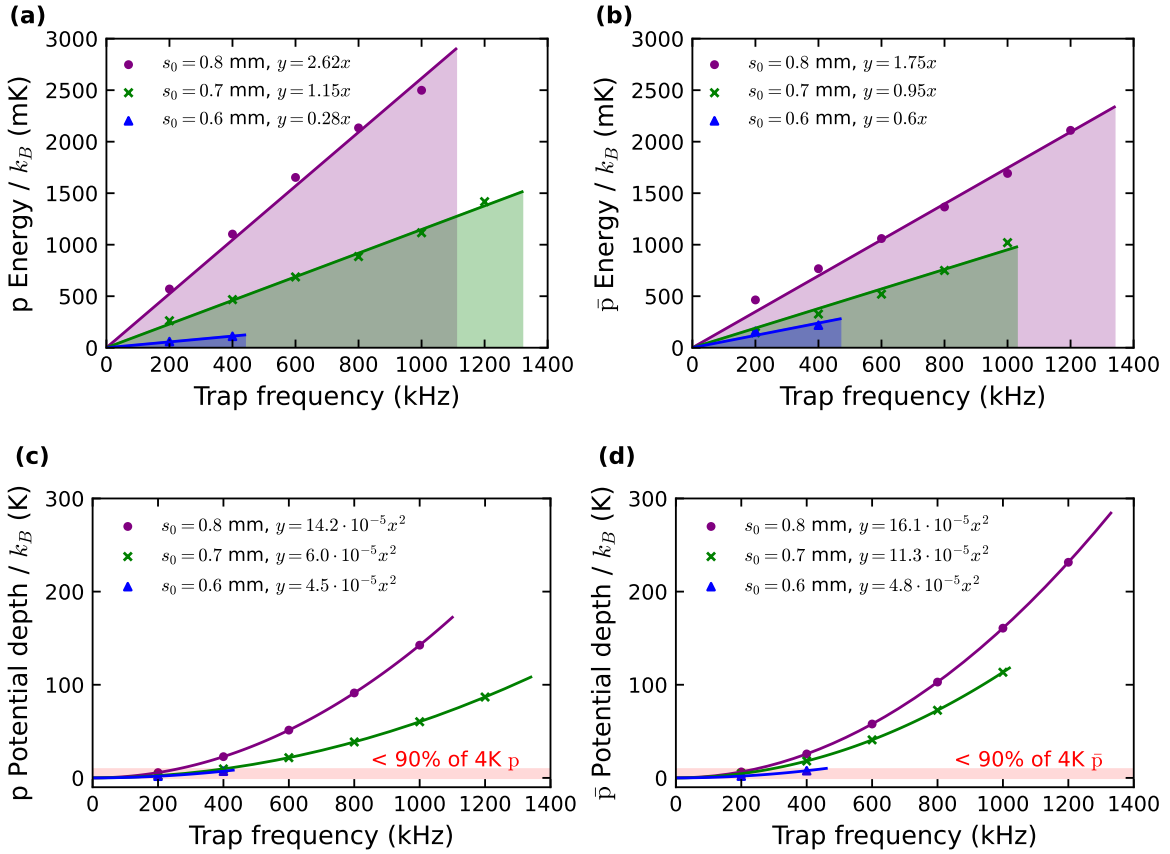


Figure 4: **Energy ranges of the double-well potential.** Harmonic energy ranges for the (a) proton and (b) antiproton, and trapping energy ranges for the (c) proton and (d) antiproton, as functions of trap frequency. Shaded regions in (a) and (b) denote initial energies from which the antiproton can be cooled below $1 \text{ mK} \times k_B$ via harmonic coupling; their upper boundaries are given by linear fits (shown in the legend), with coefficients in mK kHz^{-1} . In (c) and (d), the data are fitted quadratically (shown in the legend), with coefficients in mK kHz^{-2} . Potentials with parameters ω and s_0 above the red-shaded region trap more than 90% of 4 K (anti-)protons.

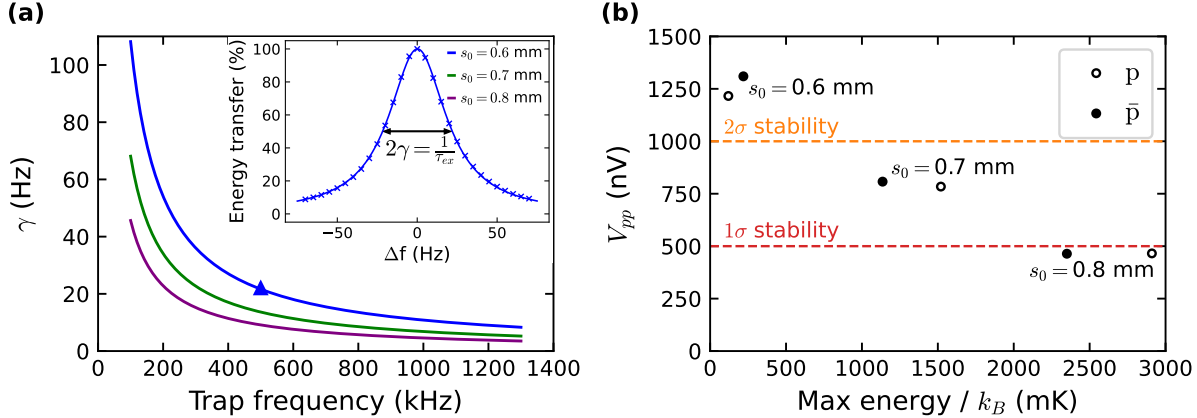


Figure 5: **Stability of the energy transfer.** **a)** Half width at half maximum (γ) of the energy transfer resonance curve as a function of the trap frequency. The plot was calculated using Eq. 4 and the relation $2\gamma = 1/\tau_{ex}$. In the top right corner, an example resonance curve for $f = 500$ kHz and $s_0 = 0.6$ mm (marked with a blue triangle) is fit to a Lorentzian function. The data are evaluated using the percentage of energy transferred from a proton oscillating at frequency f to a ${}^9\text{Be}^+$ ion oscillating at frequency $f + \Delta f$, where Δf is the deviation from the resonance frequency. **b)** Required power supply stability to achieve an 80% energy transfer. For each s_0 , the maximum initial energy of the (anti-)proton is taken from Fig. 4. The calculation of the voltage stability is described in the appendix. Dashed lines indicate a power supply stability of $V_{pp} = 0.5 \mu\text{V}_{pp}$. Data points above the 1σ stability line are expected to achieve the desired transfer at least 68.3% of the time, while those above the 2σ stability line are expected to do so at least 95.4% of the time.

s_0 allows to cool an (anti-)proton from a higher initial energy. Figs. 4c and 4d show the corresponding potential well depths, which scale quadratically with f . Consequently, larger harmonic regions are associated with deeper wells. While this suggests that larger s_0 and f are advantageous, Fig. 5a demonstrates that these conditions also result in a narrower resonance curve, imposing stricter requirements on frequency stability in the experimental implementation.

We investigate the voltage stability required to achieve an 80% energy transfer, as shown in Fig. 5b. The detailed calculations are presented in the appendix. The required stability is compared to that of a power supply with $V_{pp} = 0.5 \mu\text{V}_{pp}$, as estimated in the datasheet of the Stefan Stahl UM 1-14-LN ultrastable power supply [43]. Using a power supply with larger peak-to-peak voltage fluctuations results in a reduced fraction of transferred energy. Cooling an (anti-)proton from a higher initial energy requires a larger s_0 , which in turn again requires a higher power supply stability. Therefore, to cool the majority of the (anti-)proton energy distribution at 4 K while relaxing the stability requirements, we consider a smaller s_0 in combination with a time-varying anharmonic potential.

4.2. Frequency sweep

Due to the anharmonicities of the potential, the axial oscillation frequency of the (anti-)proton decreases with increasing axial energy. To maintain resonance with the ${}^9\text{Be}^+$ ion during coupling, we sweep the frequency of the ${}^9\text{Be}^+$ potential minimum, as shown in Fig. 6a. The sweep rate is optimized to be as fast as possible while keeping the particles in resonance. We consider $f = 500 \text{ kHz}$ and $s_0 = 0.7 \text{ mm}$, which provide a potential barrier height sufficient to trap more than 90% of 4 K (anti-)protons. We set $\Delta s_0 = 0 \text{ }\mu\text{m}$, as maximizing the harmonicity of the (anti-)proton well is not necessary for anharmonic coupling. Examples of the energy evolution are shown in Fig. 6b for the proton and in Fig. 6c for the antiproton. At the start of the sweep, while remaining off-resonance with the ${}^9\text{Be}^+$ ion, the (anti-)proton energy remains constant; once its oscillation frequency matches that of the ${}^9\text{Be}^+$ ion, its energy begins to decrease. A key advantage of the frequency-sweep method is that it does not require prior knowledge of the initial (anti-)proton energy and the maximum initial energy that can be cooled is set by the depth of the (anti-)proton potential well. For the parameters considered here, this method enables cooling of any initial energy below $9.4 \text{ K} \times k_B$ for protons and below $10.3 \text{ K} \times k_B$ for antiprotons. Experimentally, such a sweep could be implemented through a series of voltage ramps.

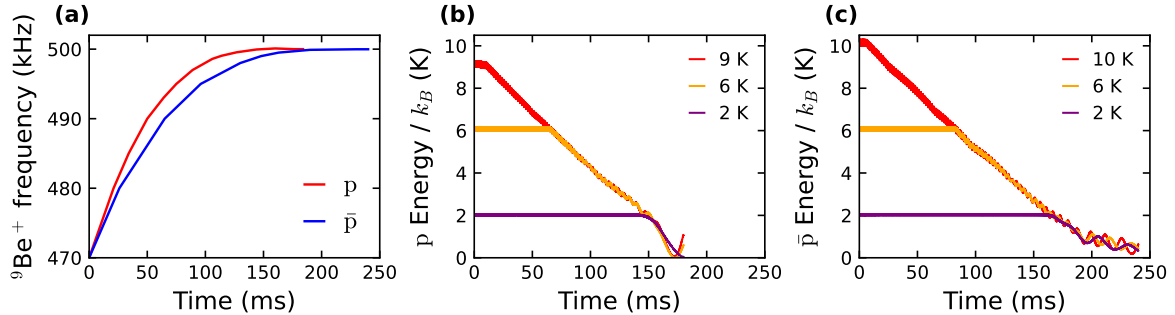


Figure 6: **Frequency sweep.** **a)** Frequency values during the sweep of the ${}^9\text{Be}^+$ ion potential, which is achieved using a series of linear voltage ramps. The sweep rate is chosen to maintain resonance between the (anti-)proton and the ${}^9\text{Be}^+$ ion throughout the sweep. Examples of the **b)** proton and **c)** antiproton energy evolution during the sweep. Voltage fluctuations are not included in these simulations.

In Fig. 7, we show the energy distributions of the (anti-)proton before and after applying the frequency sweep once and twice. We considered 1200 samples, applying voltage fluctuations to the trap electrodes in each case, following a normal distribution with a standard deviation of $\sigma_V = 250 \text{ nV}$. After two sweeps, the proton energy distribution exhibits a sharp drop at $460 \text{ mK} \times k_B$, encompassing 88% of protons. For the antiproton, the energy distribution exhibits a sharp drop at $260 \text{ mK} \times k_B$, encompassing 91% of antiprotons. Thus, following cooling by frequency sweeping, the majority of the 4 K (anti-)proton distribution can subsequently be cooled via the harmonic coupling

mechanism described in Fig. 4. The resulting energy distributions obtained without including voltage fluctuations are shown in Appendix B.

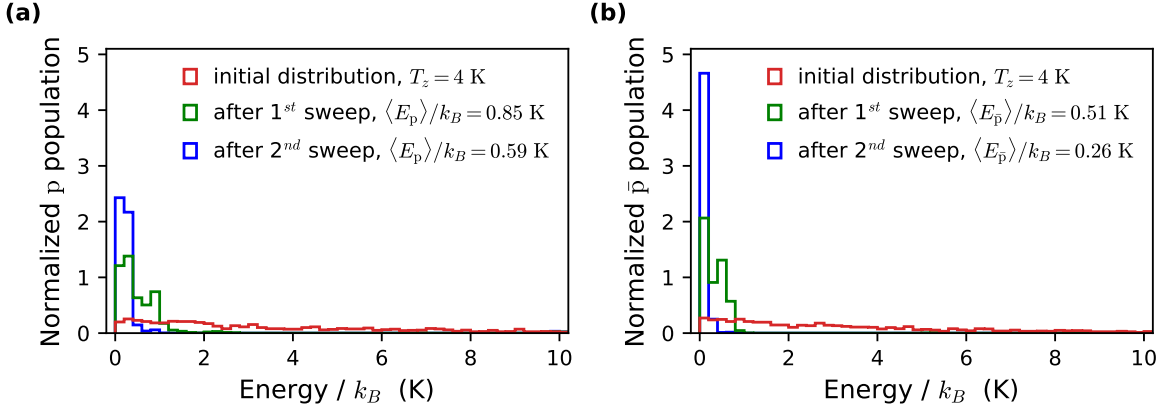


Figure 7: **Monte Carlo simulation results.** (a) Proton. (b) Antiproton. Energy distributions are shown before and after applying the frequency sweep once and twice. Each plot is based on 1200 Monte Carlo samples. Normally distributed voltage fluctuations with a standard deviation of $\sigma_V = 250$ nV were applied to all trap electrodes. All distributions are normalized such that the total area under each curve equals one. The (anti-)proton is initialized with energies drawn from a 4 K Boltzmann distribution. The temperature of the resulting distributions is extracted from the mean energy, as indicated in the legend.

4.3. Discussion

A robust scheme to cool the (anti-)proton to its motional ground state could proceed as follows:

- (i) **Initialization.** Cool the ${}^9\text{Be}^+$ ion to its motional ground state and the (anti-)proton to approximately 4 K.
- (ii) **Frequency Sweep.** Perform two frequency sweeps of the ${}^9\text{Be}^+$ potential well to cool 91 % (88 %) of antiprotons (protons) to < 260 mK (< 460 mK).
- (iii) **Harmonic Coupling.** Apply a time-independent harmonic coupling potential to cool the (anti-)proton to below 1 mK.
- (iv) **Ground-state Cooling.** Apply a time-independent harmonic coupling potential to bring the (anti-)proton to its motional ground-state, using a smaller s_0 or f than in step (iii) to enhance robustness and decrease τ_{ex} .
- (v) **Verification.** Confirm ground-state cooling by measuring the temperature of the ${}^9\text{Be}^+$ ion.

Note that steps (iii) and (iv) can be repeated multiple times, depending on the achievable energy-transfer efficiency. For example, if the transfer efficiency is 80 % then

step (iii) should be repeated at least four times, and step (iv) at least thrice. Also note that the ${}^9\text{Be}^+$ ion needs to be reinitialized in the motional ground state after each step. The duration of the (anti-)proton cooling does not impact the time budget for our QLS-based measurements [18], as it serves as an initialization procedure and it does not need to be repeated after the first successful attempt. Using Tab. 2, the total time for the ground-state cooling can be estimated. In addition to the reinitialization of the ${}^9\text{Be}^+$ ion and the transport of the particles, the total time amounts to approximately 490 ms for the proton and 580 ms for the antiproton.

Table 2: Possible trapping parameters for each cooling step that bring 88% of 4 K protons and 91% antiprotons into the motional ground state. The choice of a different f_{Be} from the particle frequency accounts for anharmonicities or follows from Eq. 5. The time column provides an estimate of the duration of each step, assuming 80 % of energy transfer at steps (iii) and (iv).

Proton					
Cooling step	f_p (kHz)	f_{Be} (kHz)	s_0 (mm)	Time (ms)	E_{fin} (mK \times k_B)
1) Sweep	500	470–500	0.7	2×180.0	< 460
2) Harmonic	400	400.023	0.7	4×29.4	< 1
3) Ground-state	100	100.144	0.6	3×4.6	Ground state
Antiproton					
Cooling step	f_p (kHz)	f_{Be} (kHz)	s_0 (mm)	Time (ms)	E_{fin} (mK \times k_B)
1) Sweep	500	470–500	0.7	2×242	< 260
2) Harmonic	450	449.968	0.6	4×20.8	< 1
3) Ground-state	100	99.856	0.6	3×4.6	Ground state

Finally, the axial heating rate in the Coupling trap needs to be taken into account for a successful cooling process. For reference, the cyclotron heating rate in the BASE analysis trap, which has a diameter of $d = 3.6$ mm, is 6 quanta/h [44]. Assuming that anomalous heating in a Penning trap scales as d^{-2} or d^{-4} [45], we estimate the heating rate in our Coupling trap to be $\lesssim 0.7$ quanta/s. Since the final cooling step can be performed within 5 ms, this heating rate can be considered negligible.

5. Conclusion

We have simulated the sympathetic cooling dynamics of single ions interacting via the Coulomb force in double-well potentials achievable in current cryogenic multi-Penning traps. This approach is directly relevant to CPT-symmetry tests in the baryonic sector, where we focus on the sympathetic cooling of an (anti-)proton using a ground-state-cooled ${}^9\text{Be}^+$ ion. We showed that the time-independent potential

alone is insufficient to efficiently cool (anti-)protons initialized at 4 K, as realistic voltage constraints and anharmonicities hinder sympathetic cooling. To overcome these limitations, we introduced a frequency-sweeping scheme that dynamically maintains resonance between the coupled particles. For the trapping parameters considered in this work, this method enables 88% of protons to reach energies below $460 \text{ mK} \times k_B$ and 91% of antiprotons to reach energies below $260 \text{ mK} \times k_B$. When followed by a time-independent harmonic coupling stage, the (anti-)proton can be cooled to its motional ground state. This method is applicable to other ion species which cannot be directly laser cooled, such as H_2^+ and $\bar{\text{H}}_2^-$ [46], and provides a viable pathway toward quantum logic spectroscopy of (anti-)particles for high-precision tests of fundamental symmetries in Penning traps.

Acknowledgments

This work was supported by PTB, LUH, and DFG through the clusters of excellence QUEST and QuantumFrontiers as well as through the Collaborative Research Center SFB1227 (DQ-mat Project-ID 274200144) and ERC StG “QLEDS”. We also acknowledge financial support from the RIKEN Pioneering Project Funding and the MPG/RIKEN/PTB Center for Time, Constants and Fundamental Symmetries. JMC acknowledges the grant “RYC2023-042535-I” funded by MICIU/AEI/10.13039/501100011033 and by “ESF+”.

References

- [1] Diedrich F, Bergquist J C, Itano W M and Wineland D J 1989 *Physical Review Letters* **62** 403 URL <https://doi.org/10.1103/PhysRevLett.62.403>
- [2] Cirac J I and Zoller P 1995 *Physical Review Letters* **74** 4091 URL <https://doi.org/10.1103/PhysRevLett.74.4091>
- [3] Wineland D, Monroe C, Itano W, Leibfried D, King B and Meekhof D 1998 *Journal of Research of the National Institute of Standards and Technology* **103** 259 ISSN 1044677X URL <https://doi.org/10.6028/jres.103.019>
- [4] Ludlow A D, Boyd M M, Ye J, Peik E and Schmidt P O 2015 *Reviews of Modern Physics* **87** 637–701 ISSN 0034-6861, 1539-0756 URL <https://doi.org/10.1103/RevModPhys.87.637>
- [5] Marshall M C, Castillo D A R, Arthur-Dworschack W J, Aeppli A, Kim K, Lee D, Warfield W, Hinrichs J, Nardelli N V, Fortier T M, Ye J, Leibbrandt D R and Hume D B 2025 *Phys. Rev. Lett.* **135**(3) 033201 URL <https://doi.org/10.1103/hb3c-dk28>
- [6] Larson D J, Bergquist J C, Bollinger J J, Itano W M and Wineland D J 1986 *Physical Review Letters* **57** 70–73 URL <https://doi.org/10.1103/PhysRevLett.57.70>
- [7] Heinzen D J and Wineland D J 1990 *Physical Review A* **42** 2977 URL <https://doi.org/10.1103/PhysRevA.42.2977>
- [8] Schmidt P O, Rosenband T, Langer C *et al.* 2005 *Science* **309** 749–752 URL <https://doi.org/10.1126/science.1114375>
- [9] Wolf F, Wan Y, Heip J C, Gebert F, Shi C and Schmidt P O 2016 *Nature* **530** 457–460 ISSN 1476-4687 URL <https://doi.org/10.1038/nature16513>
- [10] Chou C w, Kurz C, Hume D B, Plessow P N, Leibbrandt D R and Leibfried D 2017 *Nature* **545** 203–207 ISSN 1476-4687 URL <https://doi.org/10.1038/nature22338>

- [11] Micke P, Leopold T, King S A, Benkler E, Spieß L J, Schmöger L, Schwarz M, Crespo López-Urrutia J R and Schmidt P O 2020 *Nature* **578** 60–65 ISSN 1476-4687 URL <https://doi.org/10.1038/s41586-020-1959-8>
- [12] Smorra C, Blaum K, Bojtar L, Borchert M, Franke K, Higuchi T, Leefer N, Nagahama H, Matsuda Y, Mooser A, Niemann M, Ospelkaus C, Quint W, Schneider G, Sellner S, Tanaka T, Van Gorp S, Walz J, Yamazaki Y and Ulmer S 2015 *The European Physical Journal Special Topics* **224** 3055 ISSN 1951-6355, 1951-6401 URL <https://doi.org/10.1140/epjst/e2015-02607-4>
- [13] Will C *et al.* (BASE Collaboration) 2024 *Phys. Rev. Lett.* **133**(2) 023002 URL <https://doi.org/10.1103/PhysRevLett.133.023002>
- [14] Bohman M, Grunhofer V, Smorra C, Wiesinger M, Will C, Borchert M J, Devlin J A, Erlewein S, Fleck M, Gavranovic S, Harrington J, Latacz B, Mooser A, Popper D, Wursten E, Blaum K, Matsuda Y, Ospelkaus C, Quint W, Walz J and Ulmer S 2021 *Nature* **596** 514–518 ISSN 1476-4687 URL <https://doi.org/10.1038/s41586-021-03784-w>
- [15] Latacz B M *et al.* 2025 *Nature* ISSN 1476-4687 URL <https://doi.org/10.1038/s41586-025-09323-1>
- [16] Brown K R, Ospelkaus C, Colombe Y, Wilson A C, Leibfried D and Wineland D J 2011 *Nature* **471** 196–199 ISSN 1476-4687 URL <https://doi.org/10.1038/nature09721>
- [17] Harlander M, Lechner R, Brownnutt M, Blatt R and Hansel W 2011 *Nature* **471** 200–203 ISSN 0028-0836 URL <https://doi.org/10.1038/nature09800>
- [18] Cornejo J M, Lehnert R, Niemann M *et al.* 2021 *New J. Phys.* **23** 073045 URL <https://doi.org/10.1088/1367-2630/ac136e>
- [19] Nitzschke D *et al.* 2020 *Advanced Quantum Technologies* **3** 1900133 URL <https://doi.org/10.1002/qute.201900133>
- [20] Lehnert R 2016 *Symmetry* **8** 114 URL <https://doi.org/10.3390/sym8110114>
- [21] Borchert M J, Devlin J A, Erlewein S R *et al.* 2022 *Nature* **601** 53–57 ISSN 1476-4687 URL <https://doi.org/10.1038/s41586-021-04203-w>
- [22] Schneider G, Mooser A, Bohman M, Schön N, Harrington J, Higuchi T, Nagahama H, Sellner S, Smorra C, Blaum K, Matsuda Y, Quint W, Walz J and Ulmer S 2017 *Science* **358** 1081–1084 ISSN 0036-8075, 1095-9203 URL <https://doi.org/10.1126/science.aan0207>
- [23] Smorra C, Sellner S, Borchert M J *et al.* 2017 *Nature* **550** 371–374 ISSN 1476-4687 URL <https://doi.org/10.1038/nature24048>
- [24] Brown L S and Gabrielse G 1982 *Physical Review A* **25** 2423–2425 URL <https://doi.org/10.1103/PhysRevA.25.2423>
- [25] Niemann M, Meiners T, Mielke J, Borchert M J, Cornejo J M, Ulmer S and Ospelkaus C 2019 *Measurement Science and Technology* **31** 035003 ISSN 0957-0233 URL <https://doi.org/10.1088/1361-6501/ab5722>
- [26] Mielke J, Pick J, Coenders J A, Meiners T, Niemann M, Cornejo J M, Ulmer S and Ospelkaus C 2021 *Journal of Physics B: Atomic, Molecular and Optical Physics* **54** 195402 ISSN 0953-4075 URL <https://doi.org/10.1088/1361-6455/ac319d>
- [27] Cornejo J M, Brombacher J, Coenders J A, von Boehn M, Meiners T, Niemann M, Ulmer S and Ospelkaus C 2023 *Physical Review Research* **5** 033226 URL <https://doi.org/10.1103/PhysRevResearch.5.033226>
- [28] Cornejo J M, Brombacher J, Coenders J A, Von Boehn M, Meiners T, Niemann M, Ulmer S and Ospelkaus C 2024 *Physical Review Research* **6** 033233 ISSN 2643-1564 URL <https://link.aps.org/doi/10.1103/PhysRevResearch.6.033233>
- [29] Velardi L, Delle Side D, Krasa J and Nassisi V 2014 *Nucl. Instrum. Methods Phys. Res. B* **331** 20–22 ISSN 0168-583X 11th European Conference on Accelerators in Applied Research and Technology URL <https://www.sciencedirect.com/science/article/pii/S0168583X1400113X>
- [30] Wiesinger M 2023 *Sympathetic Cooling of a Single Individually-Trapped Proton in a Cryogenic Penning Trap* PhD thesis Ruprecht-Karls Universität Heidelberg MPI for Nuclear Physics, Max

- Planck Society URL <https://hdl.handle.net/21.11116/0000-000D-A678-1>
- [31] Nagahama H *et al.* 2016 *Review of Scientific Instruments* **87** 113305 ISSN 0034-6748 URL <https://doi.org/10.1063/1.4967493>
- [32] Leonhardt M *et al.* 2025 *Nature* **641** 871–875 ISSN 1476-4687 URL <https://doi.org/10.1038/s41586-025-08926-y>
- [33] Meiners T, Coenders J A, Brombacher J *et al.* 2024 *Eur. Phys. J. Plus* **139** 262 ISSN 2190-5444 URL <https://doi.org/10.48550/arXiv.2309.06776>
- [34] von Boehn M, Schaper J, Coenders J A *et al.* 2025 *Commun. Phys.* **8** 107 ISSN 2399-3650 URL <https://doi.org/10.1038/s42005-025-02031-2>
- [35] Coenders J A *et al.* Manuscript in preparation
- [36] 2025 COMSOL Multiphysics[®] version 6.2. COMSOL AB, Stockholm, Sweden. URL <https://comsol.com/>
- [37] Blakestad R B, Ospelkaus C, VanDevender A P, Wesenberg J H, Biercuk M J, Leibfried D and Wineland D J 2011 *Physical Review A* **84** 032314 URL <https://doi.org/10.1103/PhysRevA.84.032314>
- [38] Penrose R 1955 *Math. Proc. Cambridge Philos. Soc.* **51** 406–413 URL <https://doi.org/10.1017/S0305004100030401>
- [39] Verlet L 1967 *Phys. Rev.* **159** 98–103 URL <https://doi.org/10.1103/PhysRev.159.98>
- [40] Cornell E A *et al.* 1990 *Phys. Rev. A* **41**(1) 312–315 URL <https://doi.org/10.1103/PhysRevA.41.312>
- [41] Brown L S and Gabrielse G 1986 *Rev. Mod. Phys.* **58** 233–311 URL <https://doi.org/10.1103/RevModPhys.58.233>
- [42] Powell H F, Echaniz S R d, Phillips E S, Segal D M and Thompson R C 2003 *Journal of Physics B: Atomic, Molecular and Optical Physics* **36** 961–970 ISSN 0953-4075 URL <https://doi.org/10.1088/0953-4075/36/5/315>
- [43] Electronics S 2025 *UM Series Installation and User Manual, Rev. 2025c* Stahl Electronics, Mettenheim, Germany uM 1-14 (Options -LN, -SW), UM 1-32 LN, UM 1-60 LN-SW; see p. 17 URL https://www.stahl-electronics.com/devices/um/Manual_UM_LN_SW_V2025c.pdf
- [44] Borchert M J *et al.* 2019 *Phys. Rev. Lett.* **122**(4) 043201 URL <https://doi.org/10.1103/PhysRevLett.122.043201>
- [45] Goodwin J F *et al.* 2016 *Phys. Rev. Lett.* **116**(14) 143002 URL <https://doi.org/10.1103/PhysRevLett.116.143002>
- [46] Schiller S, Cornejo J M, Poljakov N, Ospelkaus C, Ulmer S and Bakalov D 2026 Submitted to *Mol. Phys.*

Appendix A. Frequency shift due to the Coulomb interaction

Here, we derive Eq. 5. In the absence of Coulomb coupling, let ω_a denote the axial oscillation frequency of particle a , and let z_a and z_b represent the displacements of particles a and b from their respective trap minima along the trap axis. The effective potential U_{eff} experienced by particle a is given by the sum of the harmonic trapping potential U_{trap} and the Coulomb interaction potential U_C due to particle b :

$$U_{\text{eff}}(z_a, z_b) = U_{\text{trap}}(z_a) + U_C(z_a, z_b) = \frac{1}{2}m_a\omega_a^2z_a^2 + \frac{1}{4\pi\epsilon_0}\frac{q_aq_b}{s_0 - z_a + z_b}. \quad (\text{A.1})$$

For small displacements $z_a, z_b \ll s_0$, the Coulomb potential can be expanded in a Taylor series around $z_a = z_b = 0$ up to second order:

$$U_C(z_a, z_b) \approx \frac{q_aq_b}{4\pi\epsilon_0s_0} \left[1 + \frac{z_a - z_b}{s_0} + \frac{(z_a - z_b)^2}{s_0^2} \right]. \quad (\text{A.2})$$

The constant term can be omitted as it does not affect the particle dynamics. The linear term corresponds to a uniform force that merely shifts the equilibrium positions and is likewise neglected. The quadratic term, however, modifies the curvature of the potential and therefore contributes to a shift in the oscillation frequency. The effective potential can thus be written as

$$U_{\text{eff}}(z_a, z_b) \approx \frac{1}{2}m_a\omega_a^2 z_a^2 + \frac{q_a q_b}{4\pi\epsilon_0 s_0^3}(z_a - z_b)^2. \quad (\text{A.3})$$

Assuming that U_{eff} remains harmonic in the vicinity of its minimum, the modified oscillation frequency ω'_a of particle a in the presence of the Coulomb interaction is obtained from

$$\omega_a'^2 = \frac{1}{m_a} \frac{\partial^2 U_{\text{eff}}}{\partial z_a^2}. \quad (\text{A.4})$$

Taking the second derivative of equation A.3 with respect to z_a and dividing by m_a yields

$$\omega_a'^2 = \omega_a^2 + \frac{2q_a q_b}{4\pi\epsilon_0 s_0^3 m_a}. \quad (\text{A.5})$$

Assuming that the Coulomb interaction induces only a small perturbation, such that $\omega'_a \approx \omega_a$, the frequency shift $\Delta\omega_a = \omega'_a - \omega_a$ can be approximated as

$$\Delta\omega_a = \frac{\omega_a'^2 - \omega_a^2}{2\omega_a} \approx \frac{q_a q_b}{4\pi\epsilon_0 s_0^3 m_a \omega_a}. \quad (\text{A.6})$$

Performing an analogous calculation for particle b yields its corresponding frequency shift $\Delta\omega_b$. The relative frequency shift between the two particles is therefore

$$\Delta\omega = \Delta\omega_a - \Delta\omega_b = \left(\frac{1}{m_a} - \frac{1}{m_b} \right) \frac{q_a q_b}{4\pi\epsilon_0 s_0^3 \omega}, \quad (\text{A.7})$$

where $\omega \approx \omega_a \approx \omega_b$ has been assumed.

Appendix B. Robustness estimation

To calculate the energy transfer stability shown in Fig. 5, we used the following approach. As illustrated in Figs. B1 and B2, we estimated the standard deviation σ_f of the frequency fluctuations, assuming they follow a normal distribution. These fluctuations arise from voltage noise applied to all trap electrodes, modeled as normally distributed with a standard deviation of $\sigma_V = 250$ nV for voltages of less than 10 V. For each data point, we considered 1000 samples of voltage fluctuations. To evaluate the resulting frequency variations, we computed the difference in the oscillation frequencies of the (anti-)proton and the ${}^9\text{Be}^+$ ion at their respective potential minima.

To quantify the robustness of the energy transfer, we estimate the value $\gamma/(2\sigma_f)$, which describes how close the coupling is to the resonance for the resonance width $\gamma = \frac{1}{2\tau_{ex}}$. Therefore, from the Lorentzian equation, we obtain that the robustness sets

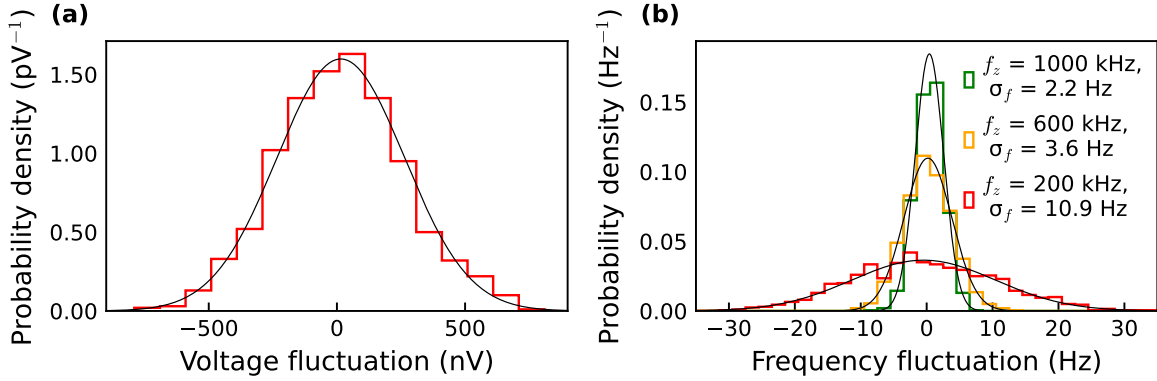


Figure B1: **Frequency fluctuations due to voltage fluctuations.** (a) Voltage fluctuations following a normal distribution with a standard deviation $\sigma_V = 250$ nV. (b) Examples of resulting frequency fluctuations for a particle separation of $s_0 = 0.7$ mm and different trap frequencies f_z . The trap frequency fluctuation are estimated from the difference between the (anti-)proton and the ${}^9\text{Be}^+$ ion at their respective potential minima. The standard deviations, σ_f , of the normal fits are shown in the legend. Each estimation of σ_f is based on a Monte Carlo simulation with 1000 samples. The data are normalized such that the area under each curve equals 1.

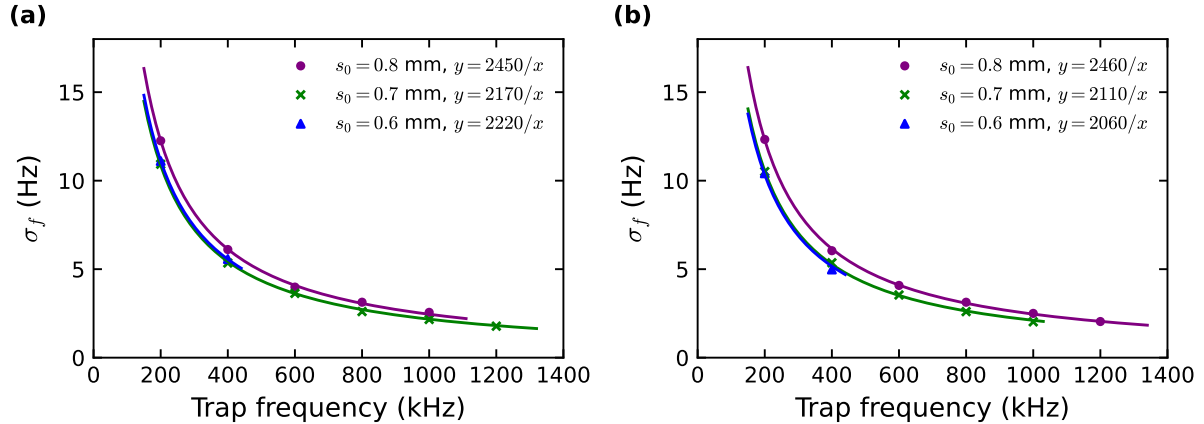


Figure B2: **Frequency fluctuation results.** a) Proton b) Antiproton. The standard deviations, σ_f , obtained from the Monte Carlo simulations as described in Fig. B1, are shown as a function of the trap frequency. The data is fit to a reciprocal function, as indicated in the legend, with coefficients in kHz \times Hz.

the fraction of energy p that can be transferred with a 95.4% confidence, given by the following equation,

$$\frac{\gamma}{2\sigma_f} = \frac{1}{\sqrt{\frac{1}{p} - 1}}. \quad (\text{B.1})$$

We show the robustness as a function of the trap frequency in Fig. B3. Since the robustness is constant with respect to the trap frequency, we only consider the maximum

initial energy E_{max} for each s_0 to describe the stability of the transfer. From Fig. 4, we find a corresponding frequency $f_{E_{max}}$ for each E_{max} . From Fig. B2, we determine the frequency fluctuation $\sigma_{f,250\text{ nV},E_{max}}$ corresponding to $f_{E_{max}}$. From Eq. B.1 we find the maximum allowed frequency fluctuation $\sigma_{f,p=0.8}$ for a $p = 0.8$ transfer. To determine the required voltage stability of the power supply, we assume that the frequency fluctuation σ_f scales linearly with the voltage fluctuation σ_V . The corresponding peak-to-peak voltage stability V_{pp} can then be expressed as

$$V_{pp} = 4 \times 250 \text{ nV} \times \frac{\sigma_{f,p=0.8}}{\sigma_{f,250\text{ nV},E_{max}}}, \quad (\text{B.2})$$

where the factor of 4 accounts for two conversions: a factor of 2 from the standard deviation σ_V to the peak-to-peak voltage V_{pp} , and another factor of 2 to convert from the 95.4% to the 68.3% confidence interval. The resulting power supply stability is shown in Fig. 5b.

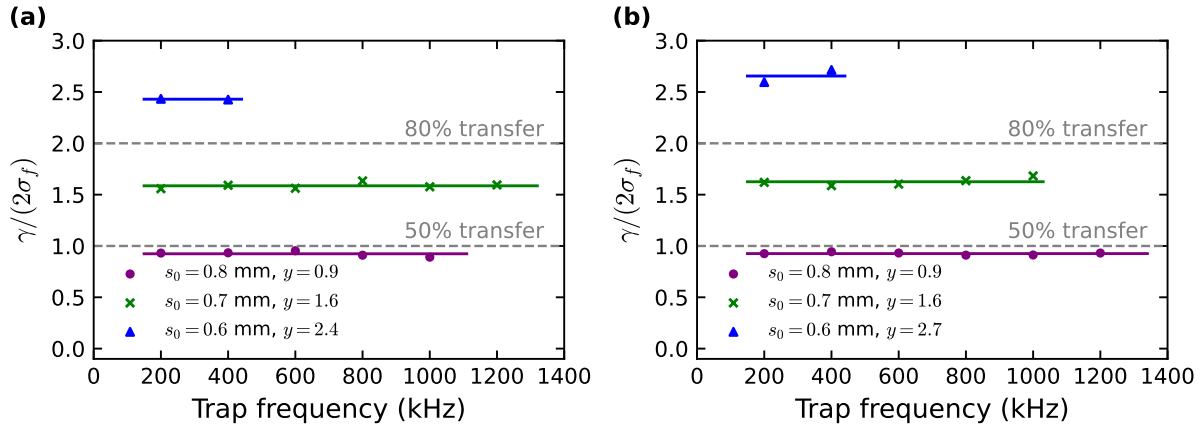


Figure B3: **Robustness of the energy transfer.** a) Proton. b) Antiproton. We quantify robustness by the ratio of the half width at half maximum, γ , from Fig. 5a, to two standard deviations in frequency fluctuations, σ_f , from Fig. B2. The ratio $\gamma/(2\sigma_f)$ determines the fraction p of the energy that can be transferred with a 95.4% confidence. The data are fit to a constant function, as indicated in the legend, with unitless coefficients. Dashed gray lines illustrate different robustness values corresponding to different p .

Fig. B4 shows the results of the frequency-sweep Monte Carlo simulations in the absence of voltage noise. After two sweeps, the proton energy distribution exhibits a sharp drop at $340 \text{ mK} \times k_B$, encompassing 89% of protons. For the antiproton, the energy distribution exhibits a sharp drop at $160 \text{ mK} \times k_B$, encompassing 91% of antiprotons. Therefore, compared to the case including voltage noise in Fig. 7, the resulting distributions are similar, indicating that the frequency-sweep technique is robust against voltage fluctuations.

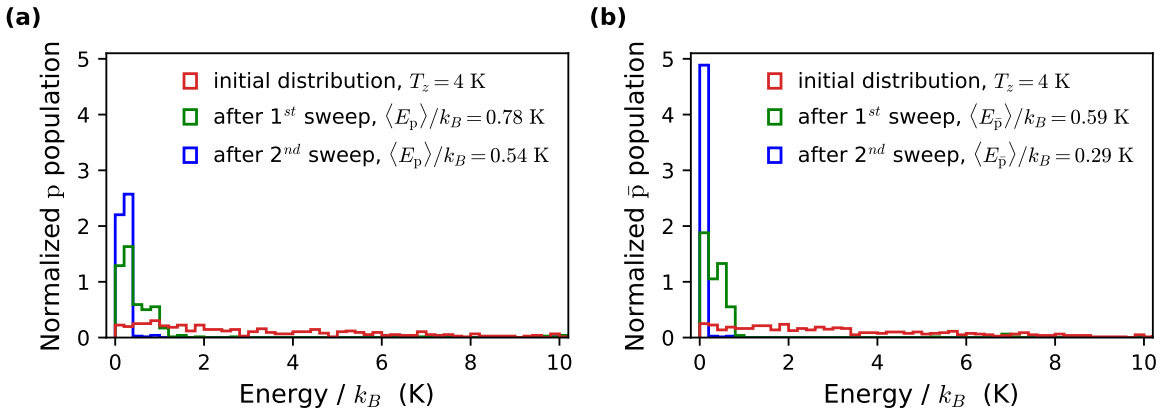


Figure B4: **Monte Carlo simulation results without voltage noise.** a) Proton. b) Antiproton. Both plots show results for 400 samples. This figure is analogous to Fig. 7, but without voltage noise applied to the trap electrodes.